Probing modified gravity with atom-interferometry

Schlogel, Sandrine; Fuzfa, André; Clesse, Sébastien

Published in:
Physical review D

DOI:
10.1103/PhysRevD.93.104036
10.1103/PhysRevD.93.104036

Publication date:
2016

Document Version
Publisher's PDF, also known as Version of record

PHYSICAL REVIEW D **93,** 104036 (2016)

Probing modified gravity with atom-interferometry: A numerical approach

Sandrine Schlögel,[1,2,*] Sébastien Clesse,[3,1,†] and André Füzfa[1,2,‡]

[1]*Namur Center of Complex Systems (naXys), Department of Mathematics, University of Namur, Rempart de la Vierge 8, 5000 Namur, Belgium*

[2]*Centre for Cosmology, Particle Physics and Phenomenology, Institute of Mathematics and Physics, Louvain University, Chemin du Cyclotron 2, 1348 Louvain-la-Neuve, Belgium*

[3]*Institute for Theoretical Particle Physics and Cosmology (TTK), RWTH Aachen University, D-52056 Aachen, Germany*

(Received 22 December 2015; published 19 May 2016)

Refined constraints on chameleon theories are calculated for atom-interferometry experiments, using a numerical approach consisting in solving for a four-region model the static and spherically symmetric Klein-Gordon equation for the chameleon field. By modeling not only the test mass and the vacuum chamber but also its walls and the exterior environment, the method allows one to probe new effects on the scalar field profile and the induced acceleration of atoms. In the case of a weakly perturbing test mass, the effect of the wall is to enhance the field profile and to lower the acceleration inside the chamber by up to 1 order of magnitude. In the thin-shell regime, results are found to be in good agreement with the analytical estimations, when measurements are realized in the immediate vicinity of the test mass. Close to the vacuum chamber wall, the acceleration becomes negative and potentially measurable. This prediction could be used to discriminate between fifth-force effects and systematic experimental uncertainties, by doing the experiment at several key positions inside the vacuum chamber. For the chameleon potential $V(\phi) = \Lambda^{4+\alpha}/\phi^{\alpha}$ and a coupling function $A(\phi) = \exp(\phi/M)$, one finds $M \gtrsim 7 \times 10^{16}$ GeV, independently of the power-law index. For $V(\phi) = \Lambda^4(1 + \Lambda/\phi)$, one finds $M \gtrsim 10^{14}$ GeV. A sensitivity of $a \sim 10^{-11}$ m/s^2 would probe the model up to the Planck scale. Finally, a proposal for a second experimental setup, in a vacuum room, is presented. In this case, Planckian values of M could be probed provided that $a \sim 10^{-10}$ m/s^2, a limit reachable by future experiments. Our method can easily be extended to constrain other models with a screening mechanism, such as symmetron, dilaton and f(R) theories.

DOI: 10.1103/PhysRevD.93.104036

I. INTRODUCTION

The accelerated cosmic expansion, highlighted by several observations such as type-Ia supernovae [1], the temperature fluctuations of the cosmic microwave background [2] and the distribution of large scale structures, has been the subject of intense research. The simplest explanation invoking a cosmological constant, in fair agreement with current observations, suffers from some fine-tuning and coincidence issues. A wide range of alternative models from various frameworks have been proposed (see e.g. [3] for a review), a lot of them introducing a dynamical scalar field coupled to matter. In order to leave observational signatures on the structure formation or the expansion history, while passing tight constraints coming from laboratory experiments [4–6], tests in the solar system (see [7] for a review, also [8,9]) and on galactic scales [10,11], a screening mechanism appears to be fruitful by suppressing the fifth-force induced by the coupled scalar field in local environments. Chameleons [12–17] are typical models where the scalar field is suppressed in a dense medium, like in the Solar System, while acting as a cosmological constant on sparse environment like in the cosmos at late time.

Many experimental tests of the chameleons have been proposed so far, involving e.g. ultracold neutrons [18–23] or cold atoms interferometry [24,25] (see also [26–31,31–34]), still leaving a part of the parameter space unconstrained. Very recently, new experiments based on atom interferometry, involving a source mass inside a vacuum chamber, have been proposed to test chameleon models with a high sensitivity [35,36], individual atoms being sufficiently small to let the scalar field unscreened even if the nucleus is dense. The experimental setup consists in measuring or constraining the additional acceleration on individual atoms, due to the scalar field gradient induced by the presence of a source mass at the center of the chamber. Forecasts were provided in [35] and first experimental results of [36] claimed to rule out most of the chameleon parameter space.

Nevertheless those results rely on analytical assumptions and have not been validated when accounting for the entire environment surrounding the experiment. In this paper, we consider a four-region model, including the wall of the chamber and the exterior environment, and we solve numerically the Klein-Gordon (KG) equation in the static

*sandrine.schlogel@unamur.be
†clesse@physik.rwth-aachen.de
‡andre.fuzfa@unamur.be

and spherically symmetric case. The only assumptions made here are (1) that the scalar field reaches its attractor (the field value at the minimum of its effective potential) outside the vacuum chamber, i.e. in the air, at spatial infinity, and (2) that we have a nonsingular C^1 solution everywhere. Our method reveals that in the regime where the test mass perturbs weakly the scalar field profile, its amplitude is controlled by the attractor outside the chamber instead of being related to the chamber size. In addition, our analysis presents the advantage of including the important effects of the vacuum chamber wall that have been neglected so far. We show that the scalar field profile and the resulting acceleration can differ by up to 1 order of magnitude in the weakly perturbing regime, compared to previous analysis [35,36]. Thus the effects of the wall cannot be neglected in a precise investigation of the chameleon parameter space. In the thin-shell regime, analytical approximations are validated to a good accuracy. Nevertheless our method highlights order of ten percents deviations. It also allows one to determine quantitatively the negative acceleration close to the walls of the vacuum chamber.

We also propose a new experimental setup, where the atom interferometer is placed inside a vacuum room. Refined constraints on the chameleon parameters (essentially the coupling function) are provided for both experimental setups and the experimental requirements to exclude the chameleon parameter space up to the Planck scale in the future are evaluated.

The numerical analysis has been performed for two typical chameleon potentials, with varying power laws. The first one (referred as Chameleon-1), $V(\phi)=\Lambda^{4+\alpha}/\phi^{\alpha}$ [37] is able to reproduce the cosmic acceleration and to fit supernovae data, however tests of general relativity in the solar system would exclude the corresponding parameter space [38]. It is nevertheless interesting to consider this model as an illustrative example of field configurations inside the vacuum chamber that are weakly perturbed by the presence of the central source mass. Laboratory experiments also probe other regions of its parameter space, even if they are not of direct interest for cosmology. The second considered potential (referred as Chameleon-2) has an additional cosmological constant [39], $V(\phi)=\Lambda^4\exp(\bar{\Lambda}^{\alpha}/\phi^{\alpha})\simeq\Lambda^4(1+\bar{\Lambda}^{\alpha}/\phi^{\alpha})$ where we assume $\Lambda=\bar{\Lambda}$ for keeping only one additional parameter, α being fixed. For both models we take an exponential coupling function $A(\phi)=\exp(\phi/M)$.

The paper is organized as follows. In Sec. II, we briefly remind the equations of motion and introduce the considered models. The experimental setup is described in Sec. III and the numerical strategy is detailed in Sec. IV. Analytical results are reminded in Sec. V and are compared to the numerical results in Sec. VI for the two considered models, refined constraints being established on their parameters. We finally discuss our results and draw some conclusions and perspectives in Sec. VII.

II. THE MODELS

We start from a generic action for modified gravity models involving a nonminimally coupled dynamical scalar field ϕ, written in the Einstein frame,

$$S=\int \mathrm{d}^4x\sqrt{-g}\left[\frac{R}{2\kappa}-\frac{1}{2}(\partial\phi)^2-V(\phi)\right]+S_m[A^2(\phi)g_{\mu\nu};\psi_{\mathrm{m}}], \tag{1}$$

with R, the scalar curvature, $\kappa=8\pi/m_{\mathrm{pl}}^2$, m_{pl} being the Planck mass, ψ_{m} the matter fields, $V(\phi)$ a general potential and $A(\phi)$ a general coupling function.

Varying this action with respect to ϕ gives the KG equation

$$\Box\phi=\frac{\mathrm{d}V}{\mathrm{d}\phi}-T\frac{\mathrm{d}\ln A}{\mathrm{d}\phi}, \tag{2}$$

where T is the trace of the energy-momentum tensor $T_{\mu\nu}=-(2/\sqrt{-g})(\partial S_{\mathrm{m}}/\partial g^{\mu\nu})$. We introduce $\tilde{T}_{\mu\nu}$ the stress-energy tensor for a perfect fluid in the Jordan frame in order to consider conserved quantities, i.e. $\tilde{\nabla}_{\mu}\tilde{T}^{\mu\nu}=0$, the tilde denoting Jordan frame quantities. Energy density ρ and pressure p in both frames are then related by [40]

$$\rho=A^4(\phi)\tilde{\rho}, \tag{3}$$

$$p=A^4(\phi)\tilde{p}, \tag{4}$$

so that in the weak field regime the KG equation in the static and spherically symmetric case becomes

$$\phi''+\frac{2}{r}\phi'=\frac{\mathrm{d}V_{\mathrm{eff}}}{\mathrm{d}\phi},\qquad \frac{\mathrm{d}V_{\mathrm{eff}}}{\mathrm{d}\phi}=\frac{\mathrm{d}V}{\mathrm{d}\phi}+\tilde{\rho}A^3\frac{\mathrm{d}A}{\mathrm{d}\phi}, \tag{5}$$

in which we have introduced an effective potential V_{eff}, the prime denoting a radial coordinate derivative. We work here in the nonrelativistic limit with negligible metric potentials and pressure. In Table I, the two considered inverse power-law chameleon potentials and the coupling function $A(\phi)$ are specified. Equations of motion for both models are identical since only the derivative of the potential $\mathrm{d}V/\mathrm{d}\phi$ contributes to the KG equation. However viable Λ values are different. For the Chameleon-1 model, Λ must be fixed by the supernovae best fit and obeys to [41]

$$\log\Lambda\approx\frac{19\alpha-47}{4+\alpha}, \tag{6}$$

in order to reproduce the acceleration of the Universe expansion even in the presence of the nonminimal coupling [38]. In the case of Chameleon-2, Λ is the cosmological

TABLE I. Characterization of the effective potential for the models of interest: potential $V(\phi)$, coupling functions $A(\phi)$, the model parameters, the minimum of the effective potential and the corresponding mass. Dependent parameters appear in brackets. Values in the last two columns are valid as long as $A(\phi) \simeq 1$ (an assumption no longer valid for some models, see discussion in Sec. VI).

	Potential $V(\phi)$	Coupling function $A(\phi)$	Parameters	Minimum of $V_{\rm eff}$ $(\phi_{\rm min})$	Mass sq. at minimum $(m^2_{\rm min})$
Chameleon 1	$\Lambda^{4+\alpha}/\phi^{\alpha}$	$e^{\phi/M}$	$(\alpha, \Lambda), M$	$(\frac{\alpha\Lambda^{\alpha+4}M}{\tilde{\rho}})^{1/(\alpha+1)}$	$\alpha(1+\alpha)\Lambda^{4+\alpha}(\frac{\tilde{\rho}}{\alpha M\Lambda^{4+\alpha}})^{\frac{2+\alpha}{1+\alpha}}$
Chameleon 2	$\Lambda^4(1+\Lambda^{\alpha}/\phi^{\alpha})$	$e^{\phi/M}$	α, Λ, M	$(\frac{\alpha\Lambda^{\alpha+4}M}{\tilde{\rho}})^{1/(\alpha+1)}$	$\alpha(1+\alpha)\Lambda^{4+\alpha}(\frac{\tilde{\rho}}{\alpha M\Lambda^{4+\alpha}})^{\frac{2+\alpha}{1+\alpha}}$

constant value $\Lambda \simeq 2.4$ meV while α is an independent variable.

III. EXPERIMENTAL SETUP

Laboratory experiments measuring the acceleration induced by a test mass can be used to probe and constrain modifications of gravity. As a reminder, the chameleon field is screened in high density environments while it mediates long-range force in sparse ones. Therefore atomic particles in an ultrahigh vacuum chamber can mimic cosmos conditions. In the first experiments, the test mass was located outside the vacuum chamber [24,25], an experimental setup which is not ideal given that the chamber wall screens the fifth force on the atoms. New experiments have been proposed in [35,36] where the test mass is located inside the vacuum chamber, which improves the constraints on the acceleration due to the scalar field. Here we focus on a recently proposed atom interferometry experiment [36] where one takes advantage of matter-wave properties of cesium-133 atoms in a Fabry-Perot cavity. When an atom absorbs/emits a photon, it recoils with a momentum $p = \hbar k$, with k the wave number of the absorbed/emitted photon. So, one can reproduce the equivalent of a Max-Zehnder interferometer for cold atoms with three light pulses using counterpropagating laser beams. Atoms are initially prepared in a hyperfine state $F = 3$ and stored in a two-dimensional magneto-optical trap. A first light pulse splits the matter-wave packet in two hyperfine states $F = 3$ and $F = 4$ and gives an impulse of $\hbar k_{\rm eff}$ to the atoms. The effective wave number $k_{\rm eff}$ depends on the two counterpropagating beam wave numbers. The probability of hyperfine transition can be controlled by the intensity and duration of both laser beams. The second pulse reverses the relative motion of the beams like the mirror of Max-Zehnder interferometer and the third pulse acts like a beam splitter which allows overlap of partial matter wave packets. Because of the recoil of the atoms, the phase difference between the two arms of the interferometer $\Delta\phi$ is a function of the acceleration a of atoms,

$$\Delta\phi = k_{\rm eff} a T^2, \tag{7}$$

where $T \sim 10$ ms in general, is the time interval between two pulses. To alleviate some systematics effects, counterpropagating laser beams are reversed and the aluminum sphere can be positioned in two places: a *near* and a *far* positions (the test mass surface is respectively located 8.8 mm and 3 cm far from the atoms), which allows to disentangle the contribution from chameleon force to Earth's gravity. One measurement consists thus of four interference fringes, corresponding to reversed counterpropagating laser beams and both positions of the test mass. Using this setup, the acceleration induced by the chameleon has been excluded up to

$$a_{\rm exp} < 5.5\ \mu{\rm m/s}^2 \quad \text{at } 95\%\,\text{C.L.} \tag{8}$$

The experimental setup proposed in [35] is similar, except that they plan to use cooled rubidium atoms launched in a small fountain located 1 cm far from the test mass. Our numerical simulations can be easily adapted for such a configuration.

Details of the considered experimental setup are reported in Table II. The size and density of the central mass, the geometry of the chamber and the vacuum density are those of [35,36]. In addition we consider the thickness and density of the vacuum chamber walls, as well as the exterior density. In Fig. 1, we draw the experimental setup considered in our numerical simulations. The four regions are labeled by their densities[1]: (1) the test mass made of aluminum (ρ_A), (2) the vacuum where the acceleration due to the chameleon is measured ($\rho_{\rm v}$), (3) the wall of the chamber ($\rho_{\rm w}$) made of stainless steel, (4) the exterior of the chamber, mostly filled by air at atmospheric pressure ($\rho_{\rm atm}$).

IV. NUMERICAL STRATEGY

Analytical approaches have been considered so far [35,36], which are valid under some assumptions like negligible chamber wall effects. Therefore, numerical methods are useful to validate and refine analytical results, by including the effects due to the experimental setup, like the thickness and the density of the wall as well as the exterior environment. In the future, numerical results will be also helpful to study more realistic situations where the vacuum chamber is not exactly spherical or cylindrical.

We consider two methods for solving the KG equation (5): a singular and multipoint boundary value

[1]In the remainder of the paper, ρ refers to the density in the Jordan frame.

TABLE II. Fiducial experimental parameters, corresponding to the setup of [36].

R_A	Radius of the test mass	1 cm/5.1×10^{13} GeV^{-1}
L	Radius of the chamber	10 cm/5.1×10^{14} GeV^{-1}
R_w	Wall thickness	1 cm/5.1×10^{13} GeV^{-1}
m_A	Test mass	11.3 g/6.7×10^{24} GeV
ρ_A	Test mass density	1.2×10^{-17} GeV^4
ρ_w	Wall density	3.5×10^{-17} GeV^4
ρ_v	Vacuum density	5.0×10^{-35} GeV^4
ρ_{atm}	Air density (P_{atm})	5.2×10^{-21} GeV^4

problem (bvp) solver with unknown parameter and a nonlinear bvp solver implementing up to sixth order a mono-implicit Runge-Kutta method with an adaptative mesh refinement, working in QUAD precision.[2] In the latter case, the density in the four regions was made continuous by considering arctan profiles with negligible widths.

We take the minimal assumption which states that the scalar field is settled to its attractor at spatial infinity, i.e. $\phi_\infty = \phi_{min}(\rho_{atm})$ as [36]. Then, the asymptotic scalar field profile is obtained by linearizing the KG equation up to first order around spatial infinity,

$$\phi'' + \frac{2}{r}\phi' = \mathcal{M}^2(\phi - \phi_\infty), \tag{9}$$

with $\mathcal{M}^2 = d^2V_{eff}/d\phi^2|_{\phi=\phi_\infty}$, which admits the Yukawa profile solution ($\mathcal{M}^2 > 0$)

$$\phi = \phi_\infty + \frac{\mathcal{C}e^{-\mathcal{M}r}}{r}, \tag{10}$$

with $\mathcal{C}$ the constant of integration. Since the KG equation is of second order and the parameter $\mathcal{C}$ is to be determined, three boundary conditions are needed. They are provided by the regularity condition on the scalar field derivative at the origin $\phi'(r = 0) = 0$ and by the asymptotic behavior of ϕ and ϕ' given by Eq. (10) at the end of the integration interval. For the multipoint bvp method, the continuity of ϕ and ϕ' are imposed at the interfaces of each region (six conditions) while the profile is guaranteed to be continuous for arctan profiles of density. The density and size of each region are reported in Table II. The two numerical methods have been checked to be in agreement with each other. Their applicability to the various regimes and their limitations in the deep thin-shell regime will be discussed in Sec. VI. We already point out that this numerical method enables one to properly account for the effect of neighboring matter on the chameleon fields and can be easily generalized to other experiments, possibly more sensitive (in the limit of spherical symmetry).

[2]For this purpose we have used the MATLAB function BVP4C which deals with singular bvp's and a modified version of the MIRKDC bvp solver with adaptative mesh in FORTRAN.

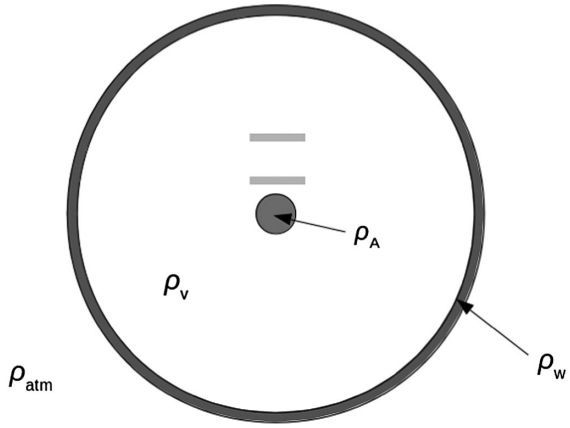

FIG. 1. Outline of the atom-interferometry experiment, simulated by a four-region model including the source mass, the vacuum chamber, its walls and the exterior environment. In light gray, the *near* and *far* positions where the acceleration on atoms is measured (note that we consider a fixed source mass to keep spherical symmetry whereas in the real experimental setup the source mass is moved [36]).

V. ANALYTICAL APPROACH

In this section we reproduce the main steps of [35] and derive analytically the chameleon field profile in the spherically symmetric and static regime for a two-region model (the source mass and the vacuum chamber). In the next section, the validity of the various assumptions will be analyzed and the analytical approximations will be compared to the exact numerical results, for the two chameleon potentials of Table I. For the sake of simplicity, we assume in this section that $\alpha = 1$.

Assuming $A(\phi) = 1$, the field value at the minimum of the effective potential written in Eq. (5), and the field mass around it, are respectively given by

$$\phi_{min} = \left(\frac{\Lambda^5 M}{\rho}\right)^{1/2}, \qquad m_{min} = \sqrt{2}\left(\frac{\rho^3}{\Lambda^5 M^3}\right)^{1/4}. \tag{11}$$

The case where the effect of $A(\phi)$ is important will be discussed in Sec. VI. For a two-region model the density ρ is either the source mass density ρ_A or the density in the vacuum chamber ρ_v.

Four different regimes can be identified, depending on whether the field reaches the effective potential minimum or not: (1) the field does not reach the minimum of the effective potential in any region, (2) the field reaches the minimum in the vacuum chamber but not in the source mass, (3) the field reaches the minimum in the source mass but not in the vacuum chamber, (4) the field reaches the minimum both inside the test mass and the vacuum chamber. Cases (1) and (2) were referred as the *weakly*

perturbing regime in Ref. [35], whereas (3) and (4) were referred as *strongly perturbing*. Below we consider those four cases separately, as in Ref. [36]. In principle, one should also distinguish between the cases where the field reaches $\phi_{\rm min}$ inside the chamber wall, or not. When lowering M, depending on the central mass density and size, on the chamber wall density and thickness, $\phi_{\rm min}$ can be reached first inside the central mass or inside the chamber walls. Nevertheless, for the considered experimental setup, the wall and the central mass have similar densities and sizes, and so those two cases will not be distinguished in the following.

A. $\phi(r=0) \neq \phi_{\rm min}(\rho_A)$ and $\phi(R_A < r < L) \neq \phi_{\rm min}(\rho_{\rm v})$

Within the test mass the field does not reach the attractor that is the minimum of the effective potential. Since $\rho_{\rm v} < \rho_{\rm atm} < \rho_{\rm A}$, the second term in the effective potential dominates, $V_{\rm eff} \simeq \phi\rho_{\rm A}/M$. The KG equation can be solved inside the mass imposing that the field profile is regular at the origin, which gives

$$\phi = D + \frac{m_{\rm A} r^2}{8\pi M R_{\rm A}^3}, \tag{12}$$

where D is an integration constant that can be fixed by matching ϕ and ϕ' to the field solution in the vacuum chamber at $r = R_A$. Inside the vacuum chamber the field does not reach the attractor value. Let us denote $\phi_{\rm bg}$ the value that would take the field at the center of the chamber in the absence of the source. Then one can consider a harmonic expansion of the potential

$$V_{\rm eff}(\phi) \simeq V_{\rm eff}(\phi_{\rm bg}) + \frac{m_{\rm bg}^2}{2}(\phi - \phi_{\rm bg})^2, \tag{13}$$

higher order terms being subdominant. One can solve the KG equation assuming that the field profile decays at infinity. This gives

$$\phi(r) = \phi_{\rm bg} + \frac{\alpha}{r} {\rm e}^{-m_{\rm bg} r}. \tag{14}$$

Note that at $r = R_A$, one has $m_{\rm bg} R_A \ll 1$ for typical experimental parameters and thus $\phi(R_A) \simeq \phi_{\rm bg} + \alpha/R_A$. After matching, one finds the field profile in case (1),

$$\phi^{(1)}(r) = \phi_{\rm bg} - \frac{m_{\rm A}}{8\pi R_{\rm A} M} \times \left[\left(3 - \frac{r^2}{R_{\rm A}^2}\right)\Theta(R_{\rm A} - r) + \left(2\frac{R_{\rm A}}{r}{\rm e}^{-m_{\rm bg} r}\right)\Theta(r - R_{\rm A}) \right], \tag{15}$$

where Θ is the Heaviside function. Therefore the effect of the mass is to deepen the field profile, by a quantity $3m_{\rm A}/(8\pi R_{\rm A} M) \ll \phi_{\rm bg}$ at $r = 0$. By definition, case (1) is valid as long as $|\phi_{\rm bg} - \phi^{(1)}(r=0)| \ll \phi_{\rm bg}$. Outside the mass, the difference $|\phi_{\rm bg} - \phi|$ decreases like $\propto 1/r$ for realistic experimental configurations where the exponential decay factor can be neglected.

A subtlety arises in the evaluation of $\phi_{\rm bg}$, which in Ref. [35] was either the attractor in the vacuum, either related to the chamber size,[3] under the assumption that the scalar field reaches the minimum of the effective potential inside the vacuum chamber wall. This assumption is actually not valid in case (1) because $\rho_{\rm w} \sim \rho_{\rm A}$, and because the wall thickness is about the radius of the test mass. So in most of the parameter space corresponding to case (1), the scalar field does not reach its attractor inside the wall. As a result, $\phi_{\rm bg}$ is better approximated by $\phi_{\rm min}(\rho_{\rm atm})$. Numerical results will highlight the effects of the chamber wall on the scalar field profile. Even if the background field value has no effect on the acceleration itself, this result is important because it changes the region in the parameter space in which case (1) applies: it is extended to lower values of M, as developed thereafter.

The analytical field profile and the induced acceleration $a_\phi = \partial_r\phi/M$ have been plotted in Figs. 2 and 3 respectively for various values of M reported in Table III.

The acceleration induced by the scalar field gradient inside the vacuum chamber is well approximated by

$$a_\phi \approx \frac{m_{\rm A}}{4\pi M^2 r}\left(\frac{1}{r} + m_{\rm bg}\right). \tag{16}$$

Since $m_{\rm bg} r \ll 1$ for realistic laboratory experiments, the acceleration is independent of Λ and thus one can constrain directly the value of M. This is the reason why, as we will show in the following, the power law of the potential has no effect on the acceleration as long as $|A(\phi) - 1| \ll 1$.

B. $\phi(0) \neq \phi_{\rm min}(\rho_A)$ and $\phi_{\rm bg} = \phi_{\rm min}(\rho_{\rm v})$

When the size of vacuum chamber is larger than the characteristic distance over which the field reaches the minimum of the potential, that is when

$$L \gg \frac{1}{m_{\rm min}(\rho_{\rm v})} = \left(\frac{\Lambda^5 M^3}{4\rho_{\rm v}^3}\right)^{1/4}, \tag{17}$$

the field profile is still governed by Eq. (15). However the value of $\phi_{\rm bg}$ is now simply $\phi_{\rm min}(\rho_{\rm v})$. In the case of the bare chameleon potential $V(\phi) = \Lambda^5/\phi$, one has $\Lambda \simeq 2.6 \times 10^{-6}$ GeV in order to reproduce the late-time accelerated

[3] $\rho_{\rm v}$ is much lower than the wall density $\rho_{\rm w}$ where the field was assumed to reach its attractor $\phi_{\rm min}(\rho_{\rm w})$. Thus the first term of $V_{\rm eff}$ in Eq. (13) dominates the KG equation inside the chamber, which can be solved to get $\phi_{\rm bg}$ as a function of the size of the vacuum chamber. However, behind this calculation is hidden the assumption that the field reaches $\phi_{\rm min}(\rho_{\rm w})$ in the wall, which is not valid in case (1) in most of the parameter space.

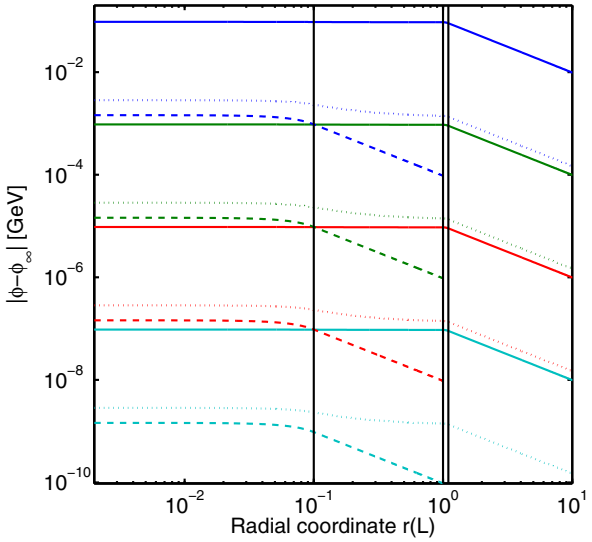

FIG. 2. Numerical and analytical scalar field profiles (respectively solid and dashed lines) in absolute value for various M listed in Table III [from top to bottom the curves correspond to increasing values of M, as reported in Table III]. The numerical profiles obtained when lowering the wall density to $\rho_w = 5 \times 10^{-19} < \rho_A$, are drawn in dotted lines, in order to illustrate that the wall density can perturb more or less importantly the field profile. Vertical lines mark out the four regions: the test mass, the chamber, the wall and outside the chamber.

expansion of the Universe. For typical vacuum densities and chamber sizes, e.g. those reported in Table II, one finds that this regime would occur when $M \lesssim 10^{-6}$ GeV. This does not correspond anymore to the weakly perturbing

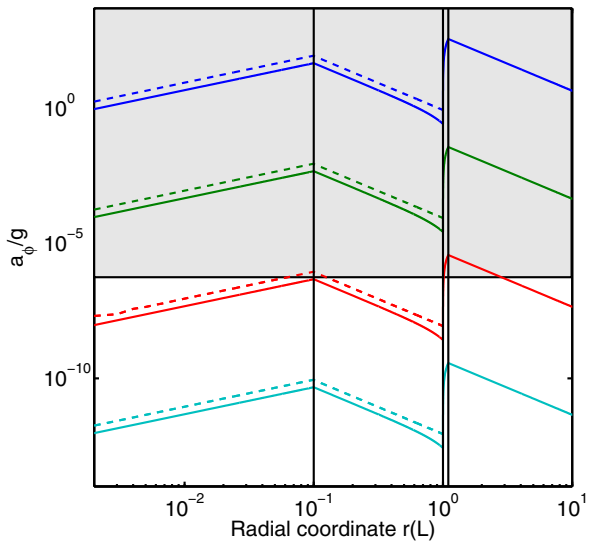

FIG. 3. Numerical and analytical profiles (respectively solid and dashed lines) of the acceleration a_ϕ/g with g the Earth gravitational acceleration, for M values listed in Table III [from top to bottom the curves correspond to increasing values of M, as reported in Table III]. Vertical lines mark out the four regions (test mass, chamber, wall and exterior).

regime requiring $\phi_{bg} \gtrsim m_A/(4\pi R_A M)$, which gives $M \gtrsim 2 \times 10^9$ GeV in our fiducial experimental setup. In the case of the potential $V(\phi) = \Lambda^4(1 + \Lambda/\phi)$, $\Lambda \simeq 10^{-12}$ GeV is the cosmological constant. It results that the field in the chamber is expected to reach $\phi_{min}(\rho_v)$ only if $M \lesssim 10^5$ GeV. There again this is far from the regime where the test mass perturbs only weakly the field, valid when $M \gtrsim 10^{20}$ GeV, i.e. in the super-Planckian regime.

C. $\phi(0) = \phi_{min}(\rho_A)$ and $\phi(R_A < r < L) \neq \phi_{min}(\rho_v)$

In case (3) the field reaches $\phi_A \equiv \phi_{min}(\rho_A)$ inside the test mass. One can define a radius S such that $\phi(S) = \phi_A(1 + \epsilon)$ with $0 < \epsilon \ll 1$. For $S < r < R_A$, the density term dominates in V_{eff} and the solution of the linearized KG equation is given by

$$\phi = D + \frac{C}{r} + \frac{m_A r^2}{8\pi M R_A^3}, \tag{18}$$

which is the same as Eq. (12) but with a nonvanishing integration constant C. Outside the test mass, the field still obeys Eq. (14). After matching ϕ and ϕ' at $r = R_A$ and ϕ at $r = S$, the integration constants α, D and C can be fixed. The resulting field profile in case (3) reads [35]

$$\phi^{(3)}(r) = \begin{cases} \phi_A, & r < S, \\ \phi_A + \frac{m_A}{8\pi R_A^3 M r}(r^3 - 3S^2 r + 2S^3), & S < r < R_A, \\ \phi_{bg} - \frac{m_A}{4\pi M r} e^{-m_{bg} r}\left(1 - \frac{S^3}{R_A^3}\right), & r > R_A, \end{cases} \tag{19}$$

with the radius

$$S \equiv R_A \sqrt{1 - \frac{8\pi M R_A \phi_{bg}}{3 m_A}} \tag{20}$$

being such that one has typically $(R_A - S)/R_A \ll 1$, corresponding to the thin-shell regime. The induced acceleration is well approximated ($m_{bg} R_A \ll 1$) by

$$a_\phi \approx \frac{m_A}{4\pi M^2 r^2}\left(1 - \frac{S^3}{R_A^3}\right) \simeq \frac{R_A \phi_{bg}}{M r^2} \tag{21}$$

and contrary to case (1), it is related to the value of ϕ_{bg}. If the wall is sufficiently large, then the field reaches $\phi_{min}(\rho_w)$ and so the calculation of ϕ_{bg} in Ref. [35] is valid, giving

$$\phi_{bg} \simeq 0.69(\Lambda^5 L^2)^{1/3} \tag{22}$$

TABLE III. Properties of the numerical scalar field and acceleration profiles for the two models in the different regimes.

Color	M [GeV]	a_ϕ/g (*near*)	a_ϕ/g (*far*)
Chameleon-1, *weakly perturbing*: Figs. 2, 3			
Blue	10^{13}	1.3×10^{1}	2.8×10^{0}
Green	10^{15}	1.3×10^{-3}	2.8×10^{-4}
Red	10^{17}	1.3×10^{-7}	2.8×10^{-8}
Light blue	10^{19}	1.3×10^{-11}	2.8×10^{-12}
Chameleon-1, *thin-shell*: Figs. 4, 5			
Blue	10^{8}	5.8×10^{9}	1.4×10^{8}
Green	10^{9}	5.2×10^{8}	5.7×10^{6}
Red	10^{10}	1.9×10^{7}	-4.4×10^{6}
Light blue	10^{11}	2.5×10^{5}	5.5×10^{4}
Chameleon-2, *thin-shell*: Figs. 9, 10			
Blue	10^{14}	5.2×10^{-7}	1.5×10^{-8}
Green	10^{15}	5.2×10^{-8}	1.5×10^{-9}
Red	10^{16}	5.2×10^{-9}	1.5×10^{-10}
Light blue	10^{17}	5.2×10^{-10}	1.5×10^{-11}
Purple	10^{18}	5.3×10^{-11}	2.4×10^{-12}
Beige	10^{19}	4.6×10^{-12}	6.8×10^{-14}

for a spherical chamber. Compared to case (1), the induced acceleration therefore does not depend only on M but also on Λ and on the size of the vacuum chamber L. When Λ is set to the cosmological constant and L to the fiducial value reported in Table II, one finds that the experiment of [36] constrains the coupling parameter down to $M\sim10^{15}$ GeV. The above calculation does not involve the power-law index α (apart indirectly via $m_{\rm bg}$, but there is no effect in the limit $m_{\rm bg}r\ll1$). Therefore it is expected that the predictions are independent of α, as long as $|A(\phi)-1|\ll1$.

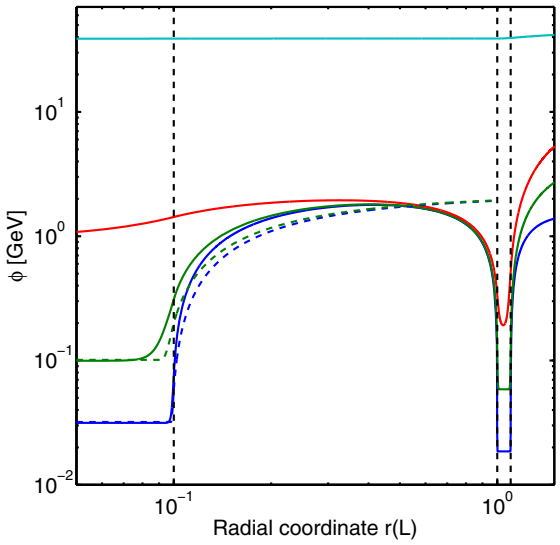

FIG. 4. Numerical results (solid lines) and analytical approximation (dashed lines) for the scalar field profile of the Chameleon-1 model, in the *strongly perturbing* (thin-shell) regime, for $\Lambda=2.6\times10^{-6}$ GeV and values of the coupling M listed in Table III [from top to bottom the curves correspond to decreasing values of M, as reported in Table III]. Differences between the two-region and four-region models are non-negligible inside the chamber, especially at the vicinity of the wall. Vertical lines mark out the four regions (test mass, chamber, wall and exterior).

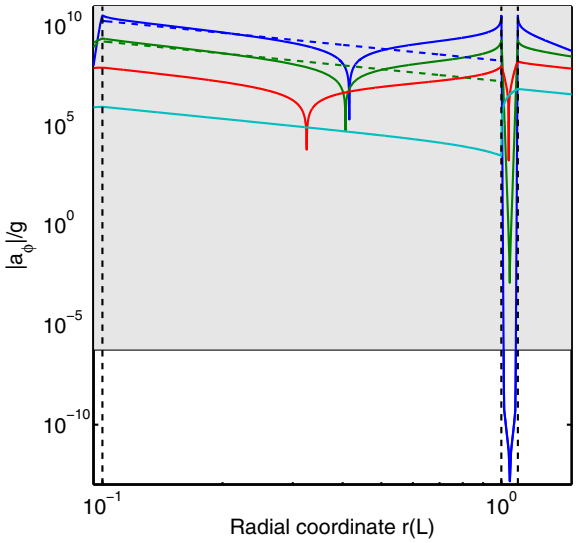

FIG. 5. Numerical results (solid lines) and analytical approximation (dashed lines) for the acceleration $|a_\phi|/g$ profile, for the same model and parameters as in Fig. 4 [from top to bottom the curves correspond to increasing values of M, as reported in Table III].The numerical profile for the four-region model shows that from the middle of the chamber to the wall, the acceleration becomes negative and increases in magnitude. Vertical lines mark out the four regions (test mass, chamber, wall and exterior).

Analytical field profiles and induced accelerations for case (3) are represented in Figs. 4 and 5 for the bare potential $V(\phi)=\Lambda^5/\phi$ (Chameleon-1), and in Figs. 9 and 10 for the potential $V(\phi)=\Lambda^4(1+\Lambda/\phi)$, for several values of M reported in Table III. Those are found to be in good agreement with the numerical results, except close to the wall where important deviations are found.

In the strongly perturbing regime, the reliability of the theory is questionable. Indeed the quantum corrections, either in the matter and the chameleon sector must remain small. Most of the parameter space reachable by the experiment proposed in [36] belongs to this regime. Following [42] the underlying instabilities are harmless and the classical analysis is trustable, keeping in mind that quantum corrections can become large at very small scales. However since the aim of this paper consists of modeling how the environment can affect the analytical results derived for the classical field, we also provide numerical forecasts in the questionable strongly perturbing regime. Nevertheless we did not explore the deeply strong regime but focus on the transition between the two regimes, where the numerical computations allow one to follow the smooth evolution of the field and acceleration profiles whereas analytical assumptions break. Our computations show that the analytical estimations are recovered once in the strong regime, and that they are quite reliable,

at least classically. The underlying quantum aspects are beyond the scope of this paper.

D. $\phi(0) = \phi_{\rm min}(\rho_A)$ and $\phi_{\rm bg} = \phi_{\rm min}(\rho_{\rm v})$

In case (4) the field profile is governed by Eq. (19) since the field reaches the effective potential minimum at the center of the test mass. However, as long as the condition Eq. (17) is satisfied, $\phi_{\rm bg} = \phi_{\rm min}(\rho_{\rm v})$. For the bare potential $V(\phi) = \Lambda^5/\phi$, case (4) takes place when $M \lesssim 10^{-3}$ GeV, whereas for the potential $V(\phi) = \Lambda^4(1 + \Lambda/\phi)$ one needs $M \lesssim 10$ GeV in order to be in the strongly perturbing regime inside the test mass. Therefore case (4) is irrelevant for values of Λ motivated by cosmology and realistic experimental configurations.

VI. FOUR-REGION MODEL: NUMERICAL RESULTS

A. Weakly perturbing regime

We discuss the weak field regime for Chameleon-1 exclusively since only case (3) of the previous section (strongly perturbing regime) is relevant for values of M below the Planck scale in the Chameleon-2 model. Allowing super-Planckian values, one actually would recover the regime where the field is only weakly perturbed by the central mass, but the induced acceleration would be far too low for being observable with future experiments.

In Fig. 2, $|\phi - \phi_\infty|$ is represented for various M values of the Chameleon-1 model, $\alpha = 1$ and $\Lambda = 2.6 \times 10^{-6}$ GeV being fixed, which corresponds to case (1) discussed in the previous section. Inside the test mass the scalar field is constant but the numerical profile roughly differs by 2 orders of magnitude compared to the analytical approximation. This difference is induced by the effect of the wall, which enhances $|\phi - \phi_\infty|$ in the vacuum chamber: the wall tends to stabilize the scalar field and gives it a kick right outside the wall shell. Note that the importance of the effect depends on the wall density and thickness. By setting $\rho_{\rm w} \ll \rho_{\rm A}$ (or by reducing the wall thickness), one tends to recover the analytical profile. Outside the chamber, the scalar field follows the Yukawa profile as imposed by the asymptotic behavior in Eq. (10).

The acceleration $a_\phi/g = \partial_r\phi/(Mg)$, with g the Earth gravitational acceleration, is plotted in Fig. 3. The general behavior of the acceleration profile obtained numerically does not differ significantly from the analytical approximation. However the chamber wall affects the amplitude of the profile with a difference growing up to 1 order of magnitude at the vicinity of the wall. This result illustrates how important it is to take into account the four regions modeling the experiment, in the weakly perturbing regime, in the view of establishing accurate constraints from atom-interferometry experiments. Given the experimental constraint on the acceleration $a_{\rm exp}/g < 5.6 \times 10^{-7}$ [36], we find that the Chameleon-1 model is excluded at 95% C.L. for $\alpha = 1$ and $M < 7 \times 10^{16}$ GeV (see Table III). An experiment controlling systematics to probe $a_\phi/g \lesssim 10^{-12}$ would rule out the model up to the Planck scale. This is close to the value $a_\phi/g \sim 10^{-11}$ given in [35] as a reachable sensitivity.

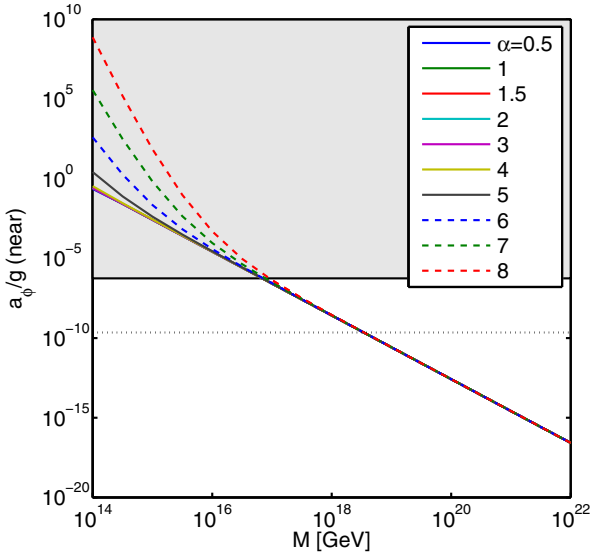

FIG. 6. Forecast for the normalized acceleration a_ϕ/g measured in the "near" position, i.e. 8.8 mm far from the test mass, for various M and α. The dotted line represents the gravitational acceleration due to the test mass.

In Fig. 6, the parameter space of (α, M) is explored for the acceleration measured in the *near* position (see Sec. III). Deviations between *near* and *far* positions are tiny (see Table III for an order of magnitude). A universal behavior with respect to α is observed for $M > 10^{17}$ GeV. Given the current bounds on a_ϕ/g, we thus find that the coupling parameter M is constrained identically for Chameleon-1 models, independently of the α power-law parameter. Future experiments will not be able to distinguish between the various power-law potentials. The universal behavior is broken at lower values of M because the assumption $|A(\phi) - 1| \ll 1$ is not valid and the analytical approach cannot be trusted anymore.

B. Strongly perturbing regime

Probing the deep thin-shell regime, i.e. when $(R_{\rm A,w} - S_{\rm A,w}) \ll R_{\rm A,w}$ (thin-shell radius of the test mass or of the chamber wall), is very challenging numerically. Up to some point, it is nevertheless possible to track the solution and to check the validity of the analytical estimations, typically using mesh refinement methods. The numerical treatment also allows one to probe the smooth transition between the weakly and strongly perturbed cases.

1. Chameleon-1

Even if one has already predicted analytically that the acceleration would be excluded, the field and acceleration

profiles have been also computed for parameters corresponding to the strongly perturbed regime, referred to as Case (3) in Sec. V. Those are represented in Figs. 4 and 5 and compared to analytical predictions for several values of M. Our numerical method also allows one to probe the transitory regime.

As expected given that $\rho_A \lesssim \rho_w$ with similar test mass radius and wall thickness, when lowering M, the field reaches first the potential minimum $\phi_{min}(\rho_w)$ inside the wall, and then $\phi_{min}(\rho_A)$ within the test mass, over a very thin radius. Inside the vacuum chamber, one observes that the field roughly reaches the amplitude of ϕ_{bg} given by Eq. (22), which validates the calculation of [35]. In the vicinity of the chamber wall, however, the acceleration changes its sign and becomes negative, with a comparable magnitude with the acceleration close to the source mass. This effect could be helpful experimentally to discriminate between a signal of modified gravity and systematic errors, by performing measurements of the acceleration at several key positions of the chamber.

2. Chameleon-2

For the Chameleon-2 model and the considered experimental setup, it has been impossible to track numerically the thin-shell regime up to the point where the acceleration would have been large enough to be observed in laboratory experiments. Nevertheless, the field and acceleration profiles are represented in Figs. 7 and 8, for $M = 10^{17}$ GeV and increasing values of ρ_w and ρ_A. The attractor field values within the test mass and the wall are reached progressively and the field variations at the borders between the four regions become more steep, as expected

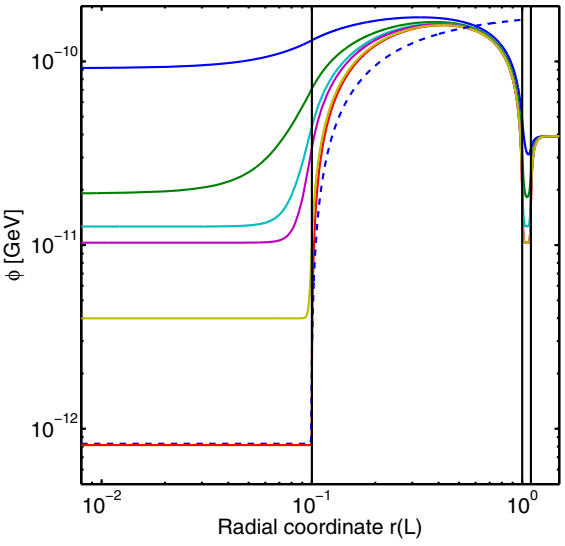

FIG. 7. Numerical results (solid lines) and analytical approximation (dashed line) for the scalar field profile of the Chameleon-2 model, for various ρ_A and ρ_w reported in Table IV, $M = 10^{17}$ GeV being fixed [from top to bottom the curves correspond to combination of parameters listed in Table IV].

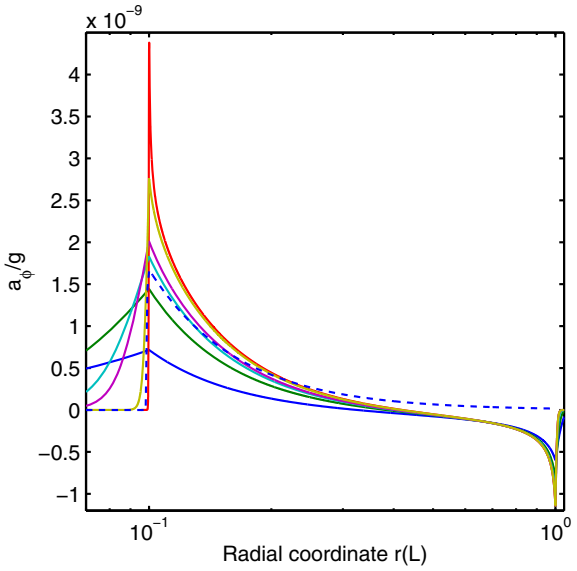

FIG. 8. Numerical results (solid lines) and analytical approximation (dashed line) for the acceleration a_ϕ/g profile of the Chameleon-2 model, for various ρ_A and ρ_w reported in Table IV, $M = 10^{17}$ GeV being fixed.

given that $(R_{A,w} - S_{A,w})/R_{A,w} \propto M\rho_{A,w}^{-1}R_{A,w}^{-2}$ [see Eq. (20)]. In the case $M = 10^{17}$ GeV, the attractor is reached inside the test mass for $\rho_A \simeq 5 \times 10^{-20}$ GeV^4, i.e. about 1000 times lower than the aluminum density, whereas inside the wall, it is reached for $\rho_w \simeq 7.5 \times 10^{-20}$ GeV^4. This slight difference is explained by the fact that the central test mass has a diameter 2 times larger than the wall thickness.

Inside the vacuum chamber, the analytical estimation is roughly recovered in the first half of the chamber. Once in the thin-shell regime, one can also observe that the field and acceleration profiles inside the chamber are independent of the wall and mass densities, except at their immediate vicinity. Therefore, in the deep thin-shell regime, the scalar field and acceleration both at the *near* and *far* positions of the interferometer do not depend on the test mass and wall densities and sizes, neither on the exterior environment. In order to obtain the numerical solution inside the chamber, down to low values of M, one can therefore use the trick to set the wall and mass densities high enough to be in the thin-shell regime but low enough for the field profile to be numerically tractable through the borders of the four regions.

The field and acceleration profiles have been calculated numerically and compared to the analytical results, for several values of M and $\Lambda \simeq 2.4$ meV. These are represented in Figs. 9 and 10. As expected the profiles have the same behavior as for the Chameleon-1 model (see Figs. 4 and 5). Close to the test mass, one recovers the analytical estimation but one can nevertheless notice differences higher than 20%.

Close to the wall, the acceleration becomes negative, and its amplitude reaches values comparable to the acceleration

TABLE IV. Densities inside the test mass ρ_A and the wall ρ_w for the numerical scalar field and acceleration profiles of Figs. 7 and 8.

Color	ρ_A [GeV^4]	ρ_w [GeV^4]
Blue	1.0×10^{-20}	1.0×10^{-20}
Green	2.5×10^{-20}	2.5×10^{-20}
Light blue	5.0×10^{-20}	5.0×10^{-20}
Purple	7.5×10^{-20}	7.5×10^{-20}
Beige	5.0×10^{-19}	7.5×10^{-20}
Red	1.2×10^{-17}	7.5×10^{-20}

at a position close to the test mass, which is a potentially measurable prediction that could be useful to discriminate between experimental systematic effects and an acceleration induced by the presence of some scalar field.

In conclusion, we find that the atom-interferometry experiment of [36] already excludes values of the coupling parameter $M \lesssim 10^{14}$ GeV at 95% C.L. Moreover, if the experimental sensitivity could be reduced down to $a_\phi/g \sim 10^{-11}$ (as it is claimed to be feasible in [35]), the model would be probed nearly up to the Planck scale. Finally, note that the typical field values reached inside the chamber are too low to induce large deviations from $A(\phi) \simeq 1$, which implies that our results are roughly independent of the power-law index α.

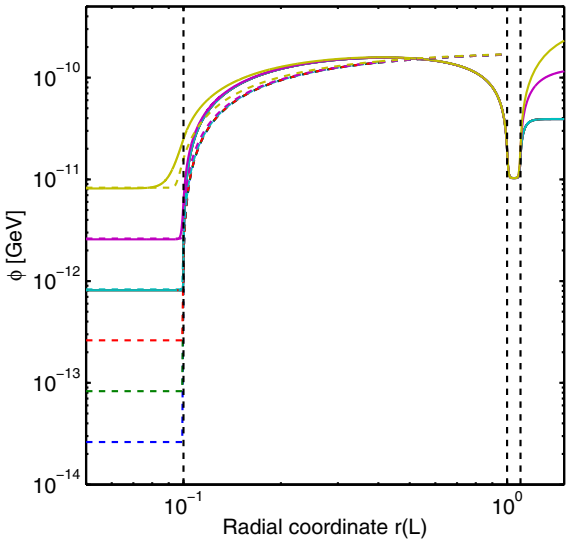

FIG. 9. Numerical results (solid lines) and analytical approximation (dashed lines) for the scalar field profile of the Chameleon-2 model, in the *strongly perturbing* (thin-shell) regime, for $\Lambda = 2.4 \times 10^{-12}$ GeV and values of the coupling M listed in Table III [from top to bottom the curves correspond to decreasing values of M, as reported in Table III]. The test mass, wall and exterior densities have been adapted for making the profile numerically tractable, with no effect inside the vacuum chamber (apart at the immediate vicinity of the borders), as explained in Sec. VI B 2. The ratios M/ρ were kept constant (with the same value as for the red curve of Fig. 7), which fixes the thin-shell radius, apart for $M = 10^{18}$ GeV (purple) and $M = 10^{19}$ GeV (beige) for which only the wall density was adapted. Noticeable deviations from the analytical estimation are observed inside the chamber, due to the wall effects. Vertical lines mark out the four regions (test mass, chamber, wall and exterior).

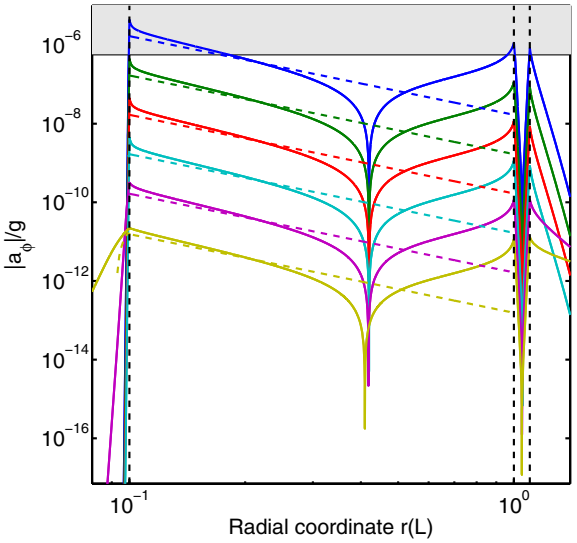

FIG. 10. Numerical results (solid lines) and analytical approximation (dashed lines) for the acceleration $|a_\phi|/g$ profile, for the same model and parameters as in Fig. 9 [from top to bottom the curves correspond to increasing values of M, as reported in Table III]. Strong discrepancies are observed between the four-region (numerical) and the two-region (analytical) models. Vertical lines mark out the four regions (test mass, chamber, wall and exterior).

C. Chamber geometry effects

The numerical method used throughout this paper takes into account the effects of the chamber geometry, in the limit where the vacuum chamber is spherical. Exploring various chamber size and wall density, we propose to consider the possibility to realize the same atom interferometry experiment in a vacuum room in order to make the test of M values up to the Planck scale possible in the near future. The largest vacuum rooms have a radius larger than $R = 10$ m and their walls made of concrete are sufficiently large for the field to reach inside its effective potential minimum. One can thus neglect the exterior of the chamber (see Sec. VI B). The vacuum room can sustain a vacuum around 10^{-6} Torr (we assume $\rho_v = 5 \times 10^{-31}$ GeV^4), low enough to prevent ϕ_{bg} to reach its effective potential minimum in vacuum.

Numerical field and acceleration profiles are reported in Figs. 11 and 12 respectively. Assuming as before $\rho_A = 1.2 \times 10^{-17}$ GeV^4, it results that a test mass of 1 cm radius only enables to probe the regime where the field does not reach ϕ_A inside the test mass (see dashed green lines in Figs. 11 and 12), the acceleration being thus poorly constrained. However, provided that the test mass

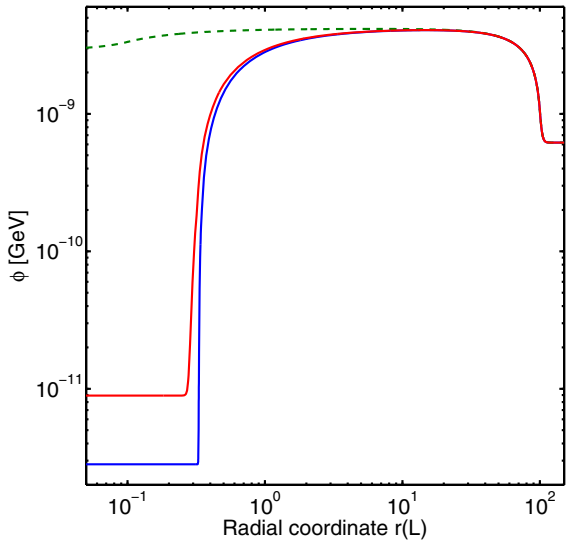

FIG. 11. Numerical scalar field profiles for a vacuum room ($L = 10$ m). The top green dashed curve is obtained for a test mass of $R_A = 1$ cm with $M = m_p$ ($\rho_w = 2.5 \times 10^{-21}$ GeV^4) while the bottom blue and the center red ones are obtained for $R_A = 3.3$ cm with $M = 0.1 \times m_p$ ($\rho_w = 2.5 \times 10^{-22}$ GeV^4) and $M = m_p$ ($\rho_w = 2.5 \times 10^{-21}$ GeV^4) respectively. We only consider a three regions model, neglecting the effect of the exterior of the vacuum room (see discussion in Sec. VI B).

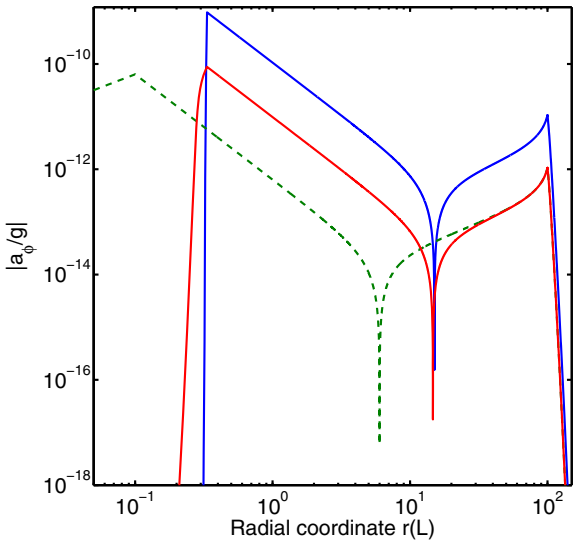

FIG. 12. Numerical acceleration profiles $|a_\phi/g|$ for a vacuum room ($L = 10$ m). The bottom green dashed curve is obtained for a test mass of $R_A = 1$ cm with $M = m_p$ ($\rho_w = 2.5 \times 10^{-21}$ GeV^4) while the top blue and the center red ones are obtained for $R_A = 3.3$ cm with $M = 0.1 \times m_p$ ($\rho_w = 2.5 \times 10^{-22}$ GeV^4) and $M = m_p$ ($\rho_w = 2.5 \times 10^{-21}$ GeV^4) respectively. We only consider a three regions model, neglecting the effect of the exterior of the vacuum room (see discussion in Sec. VI B).

radius is larger (e.g. $R_A = 3.3$ cm), the strongly perturbing regime is reached and the acceleration is large enough to be measurable in a near future for M of the order of m_{pl}. As a result, for $M = m_{pl}$, $|a_\phi|/g = 2.4 \times 10^{-10}$ at 8.8 mm from the surface of the test mass (the previously called *near* position in Sec. III) while $|a_\phi|/g = 5.7 \times 10^{-10}$ for $M = 0.1 m_{pl}$. In comparison, the test mass of 1 cm gives rise to $|a_\phi|/g = 1.7 \times 10^{-11}$ for $M = m_{pl}$.

Similarly to what was obtained in Sec. VI B, the thin-shell regime cannot be tracked numerically if the wall density is of the order of the concrete $\rho \sim 10^{-17}$ GeV^4. But one can safely consider lower values of ρ_w (see Fig. 11) without any significant change of the results inside the vacuum room.

VII. CONCLUSION

The chameleon screening mechanism is able to suppress the fifth force induced by a scalar field in locally dense environment, while allowing the scalar field to be responsible for dark energy on large astrophysical scales and thus to affect significantly the large scale structure formation. This makes chameleon theories good candidates for explaining dark energy and for being testable by future cosmology-dedicated experiments, such as Euclid [43] or the next generation of giant radiotelescopes dedicated to 21 cm cosmology [44]. Chameleon theories are also well constrained by local tests of gravity in the solar system, in the galaxy, as well as in laboratory. Recently it has been proposed to use an atom-interferometry experiment to constrain chameleon models with an unprecedented accuracy by probing the acceleration induced by the presence of the scalar field on cold atoms. The experiment is realized inside a vacuum chamber in order to reduce the screening effect, and a central mass is used to source some field gradient. Forecasts were calculated in [35] and a first experimental setup was built and used to establish new constraints on the chameleon model [36]. However the calculations of the field and acceleration profiles rely on several approximations, and until now did not fully consider the effects of the vacuum chamber wall and of the exterior environment.

The purpose of this work was to validate and refine previous calculations, by using a numerical approach consisting in solving the Klein-Gordon equation in the static and spherically symmetric case for a four-region model representing the central source mass, the vacuum chamber, its wall, and the exterior environment. Three boundary conditions are imposed: the field must be regular at origin and reach the minimum of the effective potential with a Yukawa profile, at large distance in the exterior environment. Our method allows one to probe the transition between the regime where the central source mass only weakly perturbs the field configuration, and the thin-shell regime where the field inside the central mass and inside the

chamber walls reaches the minimum of the effective potential over a very small distance. Two typical chameleon potentials were considered, in inverse power laws and allowing varying powers, as well as a standard exponential form for the coupling function.

In the weakly perturbing regime, it is found that the chamber wall enhances significantly the scalar field inside the vacuum chamber and reduces the induced acceleration, by up to 1 order of magnitude compared to previous analytical estimations and with a maximal effect close to the wall.

Going to the thin-shell regime, for our fiducial experimental setup, the field reaches the attractor inside the chamber wall and the exterior environment becomes thus irrelevant. However, for reasonable value of the induced acceleration, the field inside the vacuum chamber does not reach the minimum of the effective potential and is instead related to the size of the chamber, as first noticed in [35]. Our analysis refines the field and acceleration profiles in the chamber and highlights noticeable deviations from the analytical estimation, which is nevertheless roughly recovered close to the central test mass. Close to the chamber wall, the acceleration becomes negative, with a magnitude similar to the one close to the central mass. We argue that this prediction could be useful to distinguish between systematic effects and fifth-force effects which should be *maximal and opposite close to the central mass and to the wall*, and should vanish roughly at the middle distance between the test mass and the walls.

Refined constraints have been derived on the coupling parameter M from the atom-interferometry experiment of [36]. For the chameleon potential $V(\phi) = \Lambda^{4+\alpha}/\phi^{\alpha}$ and a coupling function $A(\phi) = \exp(\phi/M)$, one finds $M \gtrsim 7\times 10^{16}$ GeV, independently of the power law. For the bare potential $V(\phi) = \Lambda^4(1 + \Lambda/\phi)$, we find that $M \gtrsim 10^{14}$ GeV. We have also confirmed that a future experiment reducing its sensitivity down to $a \sim 10^{-10}$ m/s^2 would be able to rule out most of the parameter space of the latter model, nearly up to the Planck scale.

Finally, we have proposed to realize a similar atom-interferometry experiment inside a vacuum room. The density inside such rooms is low enough for the field profile and the induced acceleration to depend only on the size of the room. If the room radius is larger than about 10 meters, we find that the chameleon model could be probed up to the Planck scale. Nevertheless, further work is needed to implement realistic nonspherical geometries of the room (or of the vacuum chamber).

We conclude that numerical results will be helpful in the future in order to establish accurate bounds on various modified gravity models. In particular, the effects of the vacuum chamber wall and its exterior environment cannot be neglected. Our numerical method is easily extendable to study other forms of the field potential and other modified gravity models requiring a screening mechanism, such as the symmetron, dilaton and f(R) models. An investigation of the symmetron model is in progress and should be released soon. Finally it can be easily adapted to other experiments.

ACKNOWLEDGMENTS

We warmly thank Christophe Ringeval, Clare Burrage, Holger Müller, Justin Khoury, Benjamin Elder and Philipp Haslinger for useful comments and discussion. The work of S. C. is partially supported by the *Return Grant* program of the Belgian Science Policy (BELSPO). S. S. is supported by the FNRS-FRIA and A. F. is partially supported by the ARC convention No. 11/15−040.

[1] A. G. Riess *et al.* (Supernova Search Team), Astron. J. **116**, 1009 (1998).
[2] P. Ade *et al.* (Planck Collaboration), arXiv:1502.01589.
[3] L. Amendola and S. Tsujikawa, *Dark Energy: Theory and Observations* (Cambridge University Press, Cambridge, 2010).
[4] E. Adelberger (EOT-WASH Group), arXiv:hep-ex/0202008.
[5] A. Upadhye, Phys. Rev. D **86**, 102003 (2012).
[6] D. Kapner, T. Cook, E. Adelberger, J. Gundlach, B. R. Heckel, C. D. Hoyle, and H. E. Swanson, Phys. Rev. Lett. **98**, 021101 (2007).
[7] C. Will, EAS Publ. Ser. **30**, 3 (2008).
[8] V. Anastassopoulos *et al.* (CAST Collaboration), Phys. Lett. B **749**, 172 (2015).
[9] D. Scott and M. Rees, Mon. Not. R. Astron. Soc. **247**, 510 (1990).
[10] R. Pourhasan, N. Afshordi, R. Mann, and A. Davis, J. Cosmol. Astropart. Phys. 12 (2011) 005.
[11] B. Jain, V. Vikram, and J. Sakstein, Astrophys. J. **779**, 39 (2013).
[12] J. Khoury and A. Weltman, Phys. Rev. Lett. **93**, 171104 (2004).
[13] J. Khoury and A. Weltman, Phys. Rev. D **69**, 044026 (2004).
[14] S. S. Gubser and J. Khoury, Phys. Rev. D **70**, 104001 (2004).
[15] P. Brax, C. van de Bruck, A.-C. Davis, J. Khoury, and A. Weltman, Phys. Rev. D **70**, 123518 (2004).

[16] D. F. Mota and D. J. Shaw, Phys. Rev. Lett. **97**, 151102 (2006).
[17] D. F. Mota and D. J. Shaw, Phys. Rev. D **75**, 063501 (2007).
[18] T. Jenke, G. Cronenberg, J. Burgdorfer, L. Chizhova, P. Geltenbort *et al.*, Phys. Rev. Lett. **112**, 151105 (2014).
[19] H. Lemmel, Ph. Brax, A.N. Ivanov, T. Jenke, G. Pignol, M. Pitschmann, T. Potocar, M. Wellenzohn, M. Zawisky, and H. Abele, Phys. Lett. B **743**, 310 (2015).
[20] P. Brax and G. Pignol, Phys. Rev. Lett. **107**, 111301 (2011).
[21] P. Brax, G. Pignol, and D. Roulier, Phys. Rev. D **88**, 083004 (2013).
[22] A. N. Ivanov, R. Höllwieser, T. Jenke, M. Wellenzohn, and H. Abele, Phys. Rev. D **87**, 105013 (2013).
[23] P. Brax and C. Burrage, Phys. Rev. D **83**, 035020 (2011).
[24] J. Fixler, G. Foster, J. McGuirk, and M. Kasevich, Science **315**, 74 (2007).
[25] G. Lamporesi, A. Bertoldi, L. Cacciapuoti, M. Prevedelli, and G. Tino, Phys. Rev. Lett. **100**, 050801 (2008).
[26] A. Shih, Phys. Rev. A **9**, 1507 (1974).
[27] A. Shih and V. A. Parsegian, Phys. Rev. A **12**, 835 (1975).
[28] A. Anderson, S. Haroche, E. A. Hinds, W. Jhe, and D. Meschede, Phys. Rev. A **37**, 3594 (1988).
[29] C. Sukenik, M. Boshier, D. Cho, V. Sandoghdar, and E. Hinds, Phys. Rev. Lett. **70**, 560 (1993).
[30] F. Baumgärtner, R. J. Sewell, S. Eriksson, I. Llorente-Garcia, J. Dingjan, J. P. Cotter, and E. A. Hinds, Phys. Rev. Lett. **105**, 243003 (2010).
[31] D. M. Harber, J. M. Obrecht, J. M. McGuirk, and E. A. Cornell, Phys. Rev. A **72**, 033610 (2005).
[32] M. Kasevich and S. Chu, Phys. Rev. Lett. **67**, 181 (1991).
[33] A. D. Cronin, J. Schmiedmayer, and D. E. Pritchard, Rev. Mod. Phys. **81**, 1051 (2009).
[34] P. Brax, C. van de Bruck, A.-C. Davis, D. F. Mota, and D. J. Shaw, Phys. Rev. D **76**, 124034 (2007).
[35] C. Burrage, E. J. Copeland, and E. Hinds, J. Cosmol. Astropart. Phys. 03 (2015) 042.
[36] P. Hamilton, M. Jaffe, P. Haslinger, Q. Simmons, H. Müller, and J. Khoury, Science **349**, 849 (2015).
[37] B. Ratra and P. Peebles, Phys. Rev. D **37**, 3406 (1988).
[38] A. Hees and A. Fuzfa, Phys. Rev. D **85**, 103005 (2012).
[39] P. Brax, C. van de Bruck, A.-C. Davis, J. Khoury, and A. Weltman, Phys. Rev. D **70**, 123518 (2004).
[40] T. Damour and K. Nordtvedt, Phys. Rev. D **48**, 3436 (1993).
[41] C. Schimd, I. Tereno, J.-P. Uzan, Y. Mellier, L. van Waerbeke, E. Semboloni, H. Hoekstra, L. Fu, and A. Riazuelo, Astron. Astrophys. **463**, 405 (2007).
[42] A. Upadhye, W. Hu, and J. Khoury, Phys. Rev. Lett. **109**, 041301 (2012).
[43] L. Amendola *et al.* (Euclid Theory Working Group), Living Rev. Relativity **16**, 6 (2013).
[44] P. Brax, S. Clesse, and A.-C. Davis, J. Cosmol. Astropart. Phys. 01 (2013) 003.